Bioactive Materials 40 (2024) 460–473

Contents lists available at ScienceDirect

Bioactive Materials

journal homepage: www.keaipublishing.com/en/journals/bioactive-materials

Nano-vibration exciter: Hypoxia-inducible factor 1 signaling pathway-mediated extracellular vesicles as bioactive glass substitutes for bone regeneration

Zetao Wang [a,b,1], Qiyuan Dai [a,b,1], Huitong Luo [a,b], Xiyuan Han [a,b], Qi Feng [a,b,**], Xiaodong Cao [a,b,c,d,e,*]

[a] School of Materials Science and Engineering, South China University of Technology, Guangzhou, 510641, PR China
[b] National Engineering Research Centre for Tissue Restoration and Reconstruction, Guangzhou, 510006, PR China
[c] Key Laboratory of Biomedical Engineering of Guangdong Province, South China University of Technology, Guangzhou, 510006, PR China
[d] Key Laboratory of Biomedical Materials and Engineering of the Ministry of Education, South China University of Technology, Guangzhou, 510006, PR China
[e] Zhongshan Institute of Modern Industrial Technology of SCUT, Zhongshan, Guangdong, 528437, PR China

ARTICLE INFO

Keywords:
Copper-doped bioactive glass
Extracellular vesicles
HIF-1α
Bone regeneration

ABSTRACT

Bioactive glasses (BG) play a vital role in angiogenesis and osteogenesis through releasing functional ions. However, the rapid ion release in the early stage will cause excessive accumulation of metal ions, which in turn leads to obvious cytotoxicity, long-term inflammation, and bone repair failure. Inspired by the vibration exciter, small extracellular vesicles (sEVs) obtained by treating mesenchymal stem cells with copper-doped bioactive glass (CuBG-sEVs), is prepared as a nano-vibration exciter. The nano-vibration exciter can convert the ion signals of CuBG into biochemical factor signals through hypoxia-inducible factor 1 (HIF-1) signaling pathway and its activated autophagy, so as to better exert the osteogenic activity of BG. The results showed that CuBG extracts could significantly improve the enrichment of key miRNAs and increase the yield of CuBG-sEVs by activating HIF-1 signaling pathway and its activated autophagy. Cell experiments showed that CuBG-sEVs are favor to cell recruitment, vascularization and osteogenesis as the enrichment of key miRNAs. The animal experiments results showed that CuBG-sEVs stimulated angiogenesis mediated by CD31 and promoted bone regeneration by activating signaling pathways related to osteogenesis. These findings underscored the significant potential of sEVs as alternative strategies to better roles of BG.

1. Introduction

The repair of bone defects caused by trauma, infection, tumors, is a major problem in orthopedic clinics [1–3]. In the process of bone defect repair, the injured site undergoes biological processes such as vascular reconstruction, cell recruitment, and new bone formation [4–6]. Bioactive glasses (BG) not only enhance the pro-angiogenic potential of endothelial cells but also promote migration and osteogenic differentiation of bone marrow stromal cells (BMSCs), which is a kind of promising bone repair material [7,8]. Among them, Copper-doped bioactive glass (CuBG) has gained significant attention, which can release various ions that promote tissue regeneration, including copper (Cu^{2+}), calcium (Ca^{2+}) and silicon (SiO_4^{4-}) [9]. Notably, Cu^{2+} can simulate the hypoxia effects by inhibiting intranuclear and extranuclear degradation of hypoxia inducible factor 1α (HIF-1α), thereby activating the HIF-1 signaling pathway [10–12]. This activation, in turn, promote the expression of vascular endothelial growth factor (VEGF) and endothelial nitric oxide synthases (eNOS), and enhanced angiogenesis [13–15]. Moreover, CuBG can activate multiple osteogenesis-related signaling pathways, including MAPK, Wnt/β-catenin, and BMP-Smad pathways, enrich osteogenesis-related miRNAs within the cells [16]. However, the rapid ion release in the early stages can result in elevated ion concentrations

Peer review under responsibility of KeAi Communications Co., Ltd.
* Corresponding author. School of Materials Science and Engineering, South China University of Technology, Guangzhou, 510641, PR China.
** Corresponding author. School of Materials Science and Engineering, South China University of Technology, Guangzhou, 510641, PR China.
E-mail addresses: feng2119@scut.edu.cn (Q. Feng), caoxd@scut.edu.cn (X. Cao).
[1] Zetao Wang, Qiyuan Dai contributed equally to this work.

https://doi.org/10.1016/j.bioactmat.2024.06.023
Received 25 March 2024; Received in revised form 11 June 2024; Accepted 13 June 2024

and alkalinity, which leads to severe pain, hemolysis and excessive inflammatory response, thereby hindering bone regeneration [11,13,17]. Therefore, it is crucial to innovate the use of bioactive glass to avoid its side effects and better exert its biological activity.

In recent years, small extracellular vesicles (sEVs) derived from BMSCs have been considered as a safe and effective biological product, showing broad prospects in promoting bone regeneration [18,19]. It provide a potential active substance for more effectively harnessing the biological functions of CuBG. Serving as tools for cell communication, the constituents (proteins, DNA, RNAs) of sEVs depend on their cellular origin [20,21]. The sEVs are absorbed by distant cells, thereby influencing the function and behavior of these cells [20]. Among them, internal miRNAs play a crucial role in regulating intercellular communication [22,23]. Unlike direct BMSCs transplantation, sEVs inherite the advantages of source cells while avoiding their defects. It possesse homing effects, circulatory stability, and non-immunogenic molecular signals, recruiting cells and promoting tissue regeneration [23]. However, under the severe pathological conditions of bone defects, the limited production of sEVs released by BMSCs and their insufficient ability to promote vascular and bone formation restrict their clinical application. To enhance the potential and clinical applicability of sEVs in the treatment of bone defects, it is imperative to develop a strategy to promote the release of sEVs derived from BMSCs and optimize the effect of vascularized bone regeneration.

Hypoxia preconditioning of MSCs to generate high yields and activity of sEVs has been demonstrated to hold potential in the treatment of myocardial infarction, fractures, spinal cord injury, skin trauma, and osteoarthritis [24–26]. Hypoxia precondition entails exposing cells to 1–5% oxygen conditions, followed by culturing them under normal oxygen conditions and isolating sEVs post-treatment [26,27]. Cellular perception and response to oxygen in a hypoxia state were primarily regulated by the HIF-1signaling pathway and the microRNA miR-210 was a signature of hypoxia [24,28]. This signaling pathway could induce protein expression and directly or indirectly regulate multiple genes involved in cell differentiation, including VEGF, eNOS, while also inducing autophagy to enhance cellular metabolism [29,30]. Consequently, it modulated the intracellular enrichment of miRNAs related to tissue regenetaration and promoted sEVs secretion, ultimately released sEVs with high activity and yields [23,31]. Nevertheless, cells cannot be subjected to prolonged hypoxia precondition, which may adversely affect cell viability and thus may lead to apoptosis. Furthermore, pure hypoxia precondition lack specificity and make it challenging to sustainably produce sEVs that promote angiogenesis and bone regeneration. Hence, the pursuit of a mild alternative strategy, which can continuously target the intracellular HIF-1 signaling pathway for an extended period to obtain high yield and high activity sEVs, is becoming increasingly attractive.

Inspired by the operational principle of a vibration exciter, which converts received electrical energy into mechanical vibration to drive an object, we develop a novel sEVs system known as a “nano-vibration

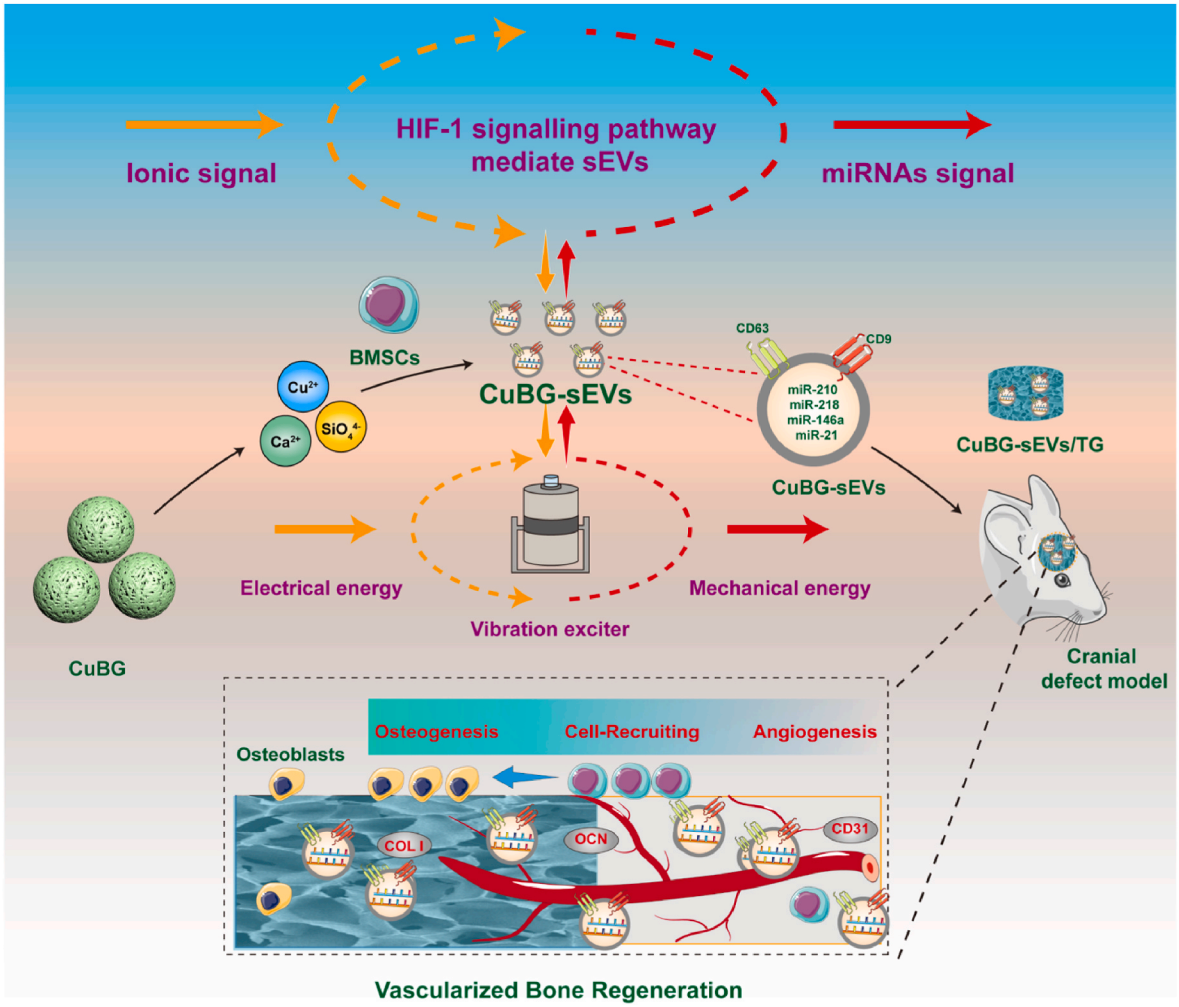

Fig. 1. Scheme of CuBG-sEVs promoting bone regeneration and repair. Simulated the effects of hypoxia were induced using CuBG to enhanced the release of high-quality sEVs derived from BMSCs. Subsequently, these sEVs were incorporated into a TG to promote angiogenesis, as depicted in the schematic diagram illustrating accelerated bone regeneration.

exciter". This nano-vibration exciter effectively converts ion signals from CuBG into miRNAs signals through HIF-1 signaling pathway, thereby driving tissues to regenerate and repair. Firstly, CuBG was used to mimic hypoxic effects by activating the HIF-1 signaling pathway to obtain sEVs (CuBG-sEVs) with high yield and enriched miRNAs. Then, CuBG-sEVs were implanted into the defect with tannic acid-coated gelatin methacryloyl cryogel (TG) and drove the defective tissue to complete the bone regeneration processes, such as angiogenesis, cell recruitment, and osteogenesis (Fig. 1).

2. Results and discussion

2.1. Extracts and characterization of sEVs

The preparation method of sEVs using CuBG was shown in Fig. 2a. Scanning electron microscopy (SEM) analysis (Fig. 2b) revealed the spherical structure of both BG and CuBG nanoparticles [11]. X-ray diffraction (XRD) analysis (Fig. S1a) confirmed that both BG and CuBG exhibited amorphous phases with characteristic BG peaks (dispersion peaks around 20–30°), with particle on average sizes of 467.31 nm and 307.48 nm (Fig. S1b). The ionic concentration results of the CuBG extracts proved the presence of Cu^{2+}, Ca^{2+}, and SiO_4^{4-} (Fig. 2c), no significant differences existed between CuBG and BG in terms of Ca^{2+} and SiO_4^{4-} release, whereas the differences between CuBG and BG in terms of bioactivity were mainly due to Cu^{2+} [32,33]. As the concentration of released phosphorous ions from bioactive glass was maintained at an exceptionally low level (0 ~ 10 ppm) and continued to decrease during the formation of hydroxyapatite, the concentrations of phosphorous ions were not measured, but focused primarily on calcium, silicon, and copper ions.These results confirmed the successful synthesis of BG ($60SiO_2$–$36CaO$–$4P_2O_5$) and CuBG ($60SiO_2$–$34CaO$–$2CuO$–$4P_2O_5$) nanoparticles. This biomaterial was recognized for its ability to stimulate angiogenesis and osteogenesis [11,13].

Subsequently, untreated sEVs derived from BMSCs was collected, as well as sEVs from BMSCs treated with BG extracts and CuBG extracts (BG-sEVs and CuBG-sEVs). Initially, the results from the Cell Counting Kit-8 (CCK8) assay showed that the proliferative capacity of BMSCs did not change significantly compared to the control group, which proved that CuBG behad decent biocompatibility (Fig. 2d). Immunofluorescence results (Fig. 2e) showed that CuBG inhibited the degradation of HIF-1α. Transmission electron microscope (TEM) analysis revealed spherical particles of sEVs measuring 40–160 nm, displaying an intact membrane structure consistent with the prototypical attributes (Fig. 2f) [34]. Particle size analysis findings (Fig. S1c) demonstrated that the size distributions of sEVs types fell within the range of 40–160 nm, consistent with the TEM analysis results. Western blot (WB) analysis demonstrated that sEVs exhibited elevated expression levels of specific marker proteins (CD63 and CD9), whereas the endoplasmic reticulum marker calnexin was not detected, suggesting that the isolation process was free from contamination with other cellular membranes (Fig. S1d) [35,36]. This suggested that CuBG treatment did not alter the size or morphology of the sEVs. The results for the concentration of sEVs was shown in Fig. 2g, and CuBG-sEVs exhibited a substantial increase. Moreover, CuBG-sEVs showed heightened potential for osteogenesis and angiogenesis (Fig. 2h), substantiated by a noteworthy elevation in miRNAs related to angiogenesis and osteogenesis (miR-210, miR-218, miR-146a and miR-21) [37–40]. Generally, CuBG-sEVs was successfully prepared with a significant increase in yield, as well as a significant increase in the

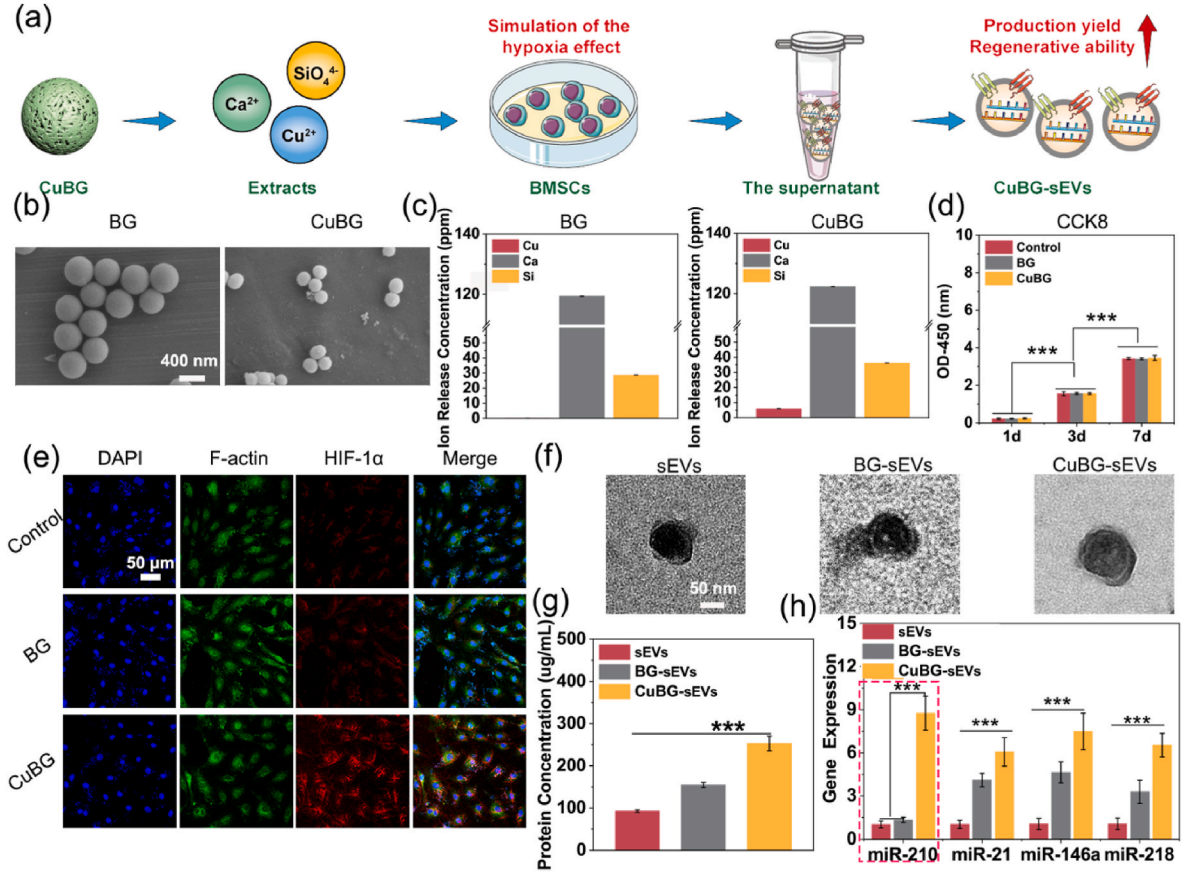

Fig. 2. Characterization of CuBG and sEVs. (a) Schematic representation of sEVs extraction. (b) SEM results of CuBG. (c) Ion release concentration of CuBG (d) CCK8 results of CuBG. (e) Immunofluorescence staining of HIF-1α protein, 4′,6-diamidino-2-phenylindole (DAPI, blue), F-actin staining (green), HIF-1α (red). (f) TEM results of sEVs. (g) Protein concentration of sEVs. (h) Detection of angiogenesis and osteogenesis related to miRNAs results inside sEVs. n = 3, $^{*}p < 0.05$, $^{**}p < 0.01$, $^{***}p < 0.001$. sEVs, untreated BMSCs-derived sEVs; BG-sEVs, BG treated BMSCs-derived sEVs. CuBG-sEVs, CuBG treated BMSCs-derived sEVs.

abundance of angiogenesis-related miRNAs in their contents.

Recently, researches about hypoxia precondition of MSCs have attracted much attention [24,27]. These studies involved treating cells for a short period of time in the range of 1–5% oxygen concentration, which promoted the secretion of highly active sEVs [41]. HIF-1 signaling pathway was a key pathway for cellular adaptation to hypoxia environments [42,43]. Under normoxic conditions, HIF-1α was hydroxylated and degraded by PHD with FIH-1 [44,45]. However, hypoxia precondition of MSCs may cause potentially undesirable cellular consequences such as apoptosis and insufficient targeting of miRNAs against angiogenesis and osteogenesis. In recent years, it has been reported that Cu^{2+} released from CuBG stabilizes HIF-1α protein by inhibiting extra-nuclear PHD induced hydroxylation of proline residues and inhibits intranuclear FIH-1 [11]. Furthermore, Cu^{2+} is an essential trace element in the process of HIF-1α-specific promotion of the expression of a series of angiogenesis-related factors [15]. In the present study, the

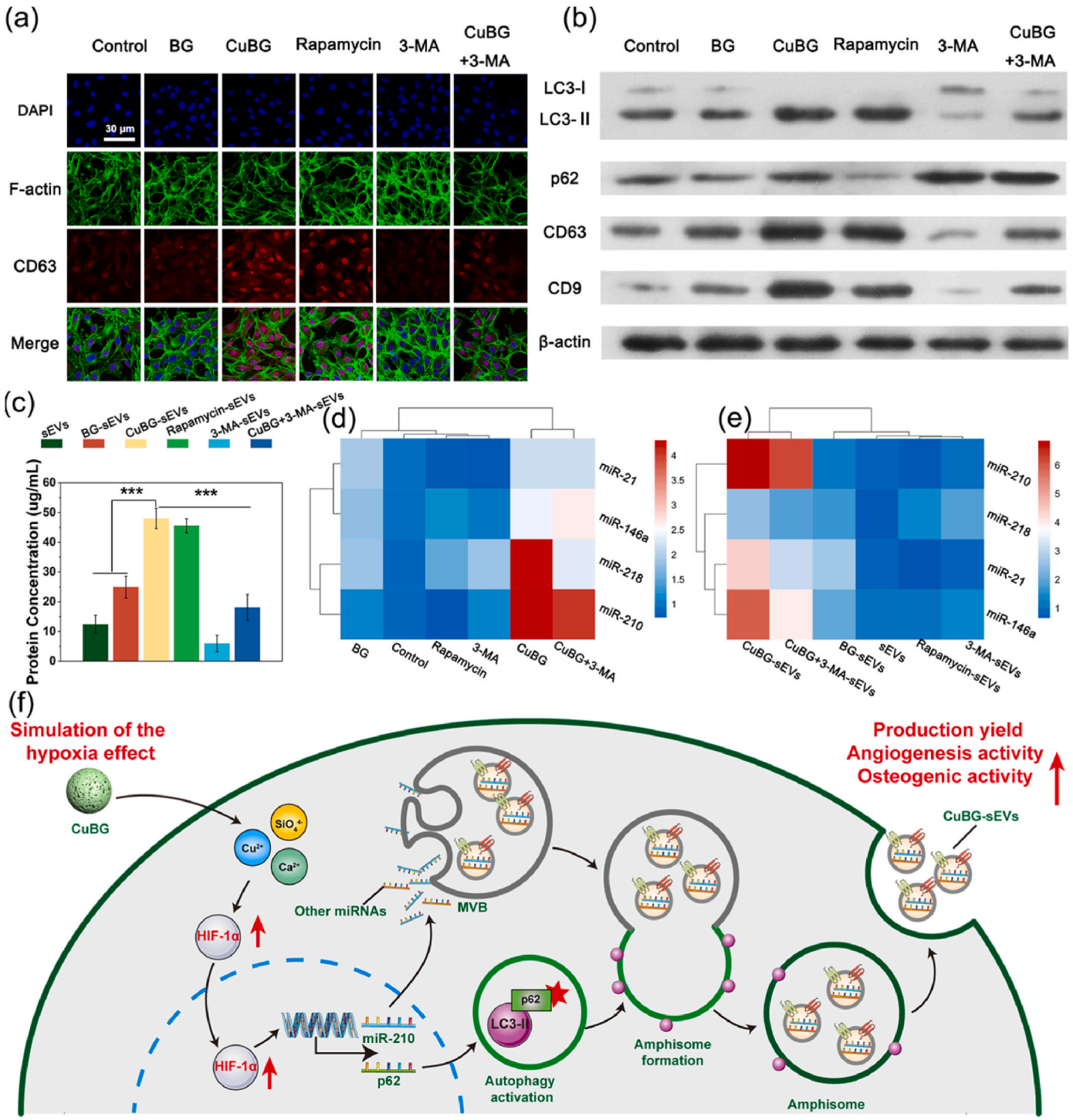

Fig. 3. Autophagic activity of BMSCs after CuBG treatment. (a) Immunofluorescence staining of CD63. (b) LC3, p62, CD63 and CD9 expression by the WB method. (c) Concentration of sEVs. (d) miRNAs expression in BMSCs. (e) miRNAs expression within sEVs. (f) Mechanistic diagram of CuBG simulated the effects of hypoxia interactions with BMSCs. n = 3, $^{*}p < 0.05$, $^{**}p < 0.01$, $^{***}p < 0.001$. Control, without sEVs; sEVs, untreated BMSCs-derived sEVs; BG-sEVs, BG treated BMSCs-derived sEVs. CuBG-sEVs, CuBG treated BMSCs-derived sEVs.

treatment with CuBG extract was a more convenient, scalable, and safe method compared with the hypoxia precondition. The advantage of this method was the ability to circumvent potential adverse effects common to traditional hypoxia culture methods. CuBG extracts significantly increased the concentration of sEVs by approximately 2.8-fold compared to the untreated or BG-treated groups. The miRNAs content analysis showed that CuBG-sEVs exhibited more abundant angiogenesis and osteogenesis-associated miRNAs compared to the untreated group. Espacially, miR-210, which targeted the HIF-1 signaling pathway, showed a substantial up-regulation compared to the BG-treated group, implying that CuBG-sEVs held significant promise in promoting vascular bone regeneration. In conclusion, CuBG could promote the secretion of sEVs and increase osteogenesis and angiogenesis-related miRNAs expression via HIF-1 signaling pathway.

2.2. Mechanism underlying the augmented production and osteogenic activity of CuBG-sEVs

The HIF-1 signalling pathway is closely linked to autophagy [46,47]. It has been demonstrated that under hypoxia conditions, HIF-1α enters the nucleus, activates the autophagy-related gene microtubule-related protein 1 light chain 3 (LC3) and beclin1, and induces the expression of p62, thereby regulating the activation of autophagy [46,48]. Hence, to further explore the mechamism of CuBG on promotion of sEVs secretion and miRNAs enrichment via the HIF-1 signaling pathway, autophagic activity was assessed by evaluating the expression of LC3-II and p62, which was a marker indicative of autophagy [49]. Furthermore, rapamycin was employed as an autophagy activator and 3-methyladenine (3-MA) was employed as an autophagy inhibitor [50]. CD63 protein, as a sEVs surface marker [20], was detected through immunofluorescence staining (Fig. 3a, Fig. S2a). An increase in CD63 stained sEVs was observed in the CuBG extract and rapamycin-treated groups, while a significant reduction was observed in the 3-MA treated group. Additionally, the impact of CuBG on autophagy was confirmed by assessing the protein expression of LC3-II (Fig. 3b, Figs. S2b–e). The outcomes indicated that CuBG enhanced the expression of CD63 and LC3-II in BMSCs, whereas 3-MA nullified the impact of CuBG extract treatment. Moreover, the BCA protein assay results substantiated the notion that CuBG-sEVs experienced a significant reduction in the CuBG extract group when autophagy was inhibited (Fig. 3c). It was clarified that CuBG-sEVs mainly increased sEVs yield by HIF-1 signaling pathway-acticited autophagy. To delve into the potential impact of CuBG extracted on miRNAs changes in BMSCs, the expression of miRNAs related to bone formation and angiogenesis in both intracellular and sEVs (Fig. 3d) was examined. Notably, CuBG treatment resulted in a significant increase in internal miRNAs within BMSCs. Conversely, rapamycin and 3-MA did not exhibit a substantial effect. Furthermore, the expression of related miRNAs in sEVs (Fig. 3e) showed a notable up-regulation in miRNAs expression within CuBG-sEVs compared to the sEVs and BG-sEVs groups. The influence of rapamycin and 3-MA on the expression of related miRNAs within sEVs aligned with their intracellular expression patterns. In conclusion, HIF-1 signaling pathway-acticited autophagy did not affect osteogenic and angiogenic-associated miRNAs expression in sEVs.

In summary, Fig. 3d and e showed that CuBG facilitated the secretion of sEVs from BMSCs and modulate miRNAs composition within sEVs. This effect appears to be linked to the release of ions, including Cu^{2+}, Ca^{2+}, and $SiO4^{4-}$, as well as the modulation of the HIF-1 signaling pathway and its activated autophagy (Fig. 3f). Specifically, Cu^{2+} activated the HIF-1 signaling pathway by inhibiting the degradation of nuclear and extra-nuclear HIF-1α, leading to an increased expression of angiogenic miRNAs, notably miR-210 [14]. Concurrently, the accumulation of HIF-1α activated p62, facilitating autophagy and augmenting the secretion of sEVs [46,51]. CuBG also released other reactive ions, such as Ca^{2+} and SiO_4^{4-}, promoting the secretion of osteogenesis-related miRNAs, such as miR-218, miR-146a and miR-21 [52,53]. Ultimately, CuBG utilized the HIF-1 signaling pathway and its activated autophagy as the primary regulatory mediators to enhance the production and osteogenic activity of CuBG-sEVs.

2.3. Angiogenesis and osteogenesis in vitro

To assess the impact of CuBG-sEVs on human umbilical vein endothelial cells (HUVECs) for promoting angiogenesis, a regimen involving the application of CuBG-sEVs to HUVECs was executed. Initially, the immunofluorescence results demonstrated the internalization capacity of sEVs by HUVECs (Fig. 4a). Subsequent transwell experiments were conducted (Fig. 4b–S3a-b) and corroborated that sEVs effectively facilitated the migration of HUVECs in contrast to the control group. Notably, CuBG-sEVs exhibited exhibiting 1.2-fold higher recruited cell numbers than BG-sEVs and 6.8-fold higher than the control group, likely attributed to the heightened expression of miR-210. The miR-210-modulated HIF-1α signaling pathway results in VEGF release, subsequently induces SDF-1 chemokine expression, thereby facilitates cell recruitment [54]. The evaluation of gene expression related to angiogenesis, including HIF-1α, VEGF, eNOS, and kinase insert domain receptor (KDR), revealed a significant up-regulation within CuBG-EVs treated cells compared to those treated with other sEVs. This was confirmed through quantitative reverse transcription PCR (RT−qPCR) analysis (Fig. 4c). Remarkably, the CuBG-sEVs were heightened (Fig. 4d–S3c). Immunofluorescence detection indicated a significant increase in platelet endothelial cell adhesion molecule (CD31) expression within the CuBG-sEVs group for 3 days. Furthermore, matrigel angiogenesis assessment showed strong cellular connectivity and formation of distinctive tubular structures within the CuBG-sEVs group (Fig. 4e), demonstrating its ability to promote angiogenesis. Moreover, the number of angiogenic vessels and the length of the vessels in the CuBG-sEVs group were significantly increased compared with the other groups (Fig. 4f and g). From the above results, it was observed that CuBG-sEVs could be internalized, recruit HUVECs and promote the expression of angiogenesis-related genes and tube formation.

To explore the osteogenic potential of CuBG-sEVs, BMSCs were cultured using CuBG-sEVs enriched medium. Initially, the ability of all three sEVs types to be internalized by BMSCs was confirmed using immunofluorescence results (Fig. 5a), along with their ability to recruit BMSCs (Fig. 5b). Subsequently, osteogenesis-related genes, including alkaline phosphatase (ALP), runt-related transcription factor (RUNX2), osteocalcin (OCN), recombinant human bone morphogenetic protein 2 (BMP2), and collagen type I alpha 1 (COL1A1), were significantly upregulated (Fig. 5c–S3d). Additionally, CuBG-sEVs promoted osteogenesis, and was assessed through ALP staining/activity and alizarin red staining (ARS)/activity (Fig. 5d–g). Similar to HUVEVs, CuBG-sEVs could also act on BMSCs, and significantly promoted the expression of osteogenesis-related genes, up-regulation of ALP activity and mineralized matrix content in vitro.

Angiogenesis played a pivotal role in bone formation by ensuring the delivery of essential nutrients, minerals, growth factors, and oxygen necessary for tissue regeneration [55–57]. The results showed that, except for the control group, CuBG-sEVs demonstrated the capacity to be internalized and stimulate HUVECs migration, highlighting the potential for intercellular communication. Notably, CuBG-sEVs upregulated HIF-1α gene expression by approximately tenfold in 7 days, in contrast to the sEVs group lacking miR-210 and the BG-sEVs group. Additionally, CuBG-sEVs significantly increased the expression of VEGF, KDR, and eNOS. It also exhibited pronounced expression of the vascular marker CD31 and demonstrated a substantial enhancement in their vascular formation capacity [58]. miR-210 activated the HIF-1 signaling pathway, thereby promoting the expression of vital downstream genes involved in vascular development. The recruitment and osteogenesis of native MSCs was extremely important for bone regeneration. CuBG-sEVs were rich in miRNAs related to osteogenesis, such as miR-218, miR-146a and miR-21, suggesting strong osteogenic potential. This hypothesis was

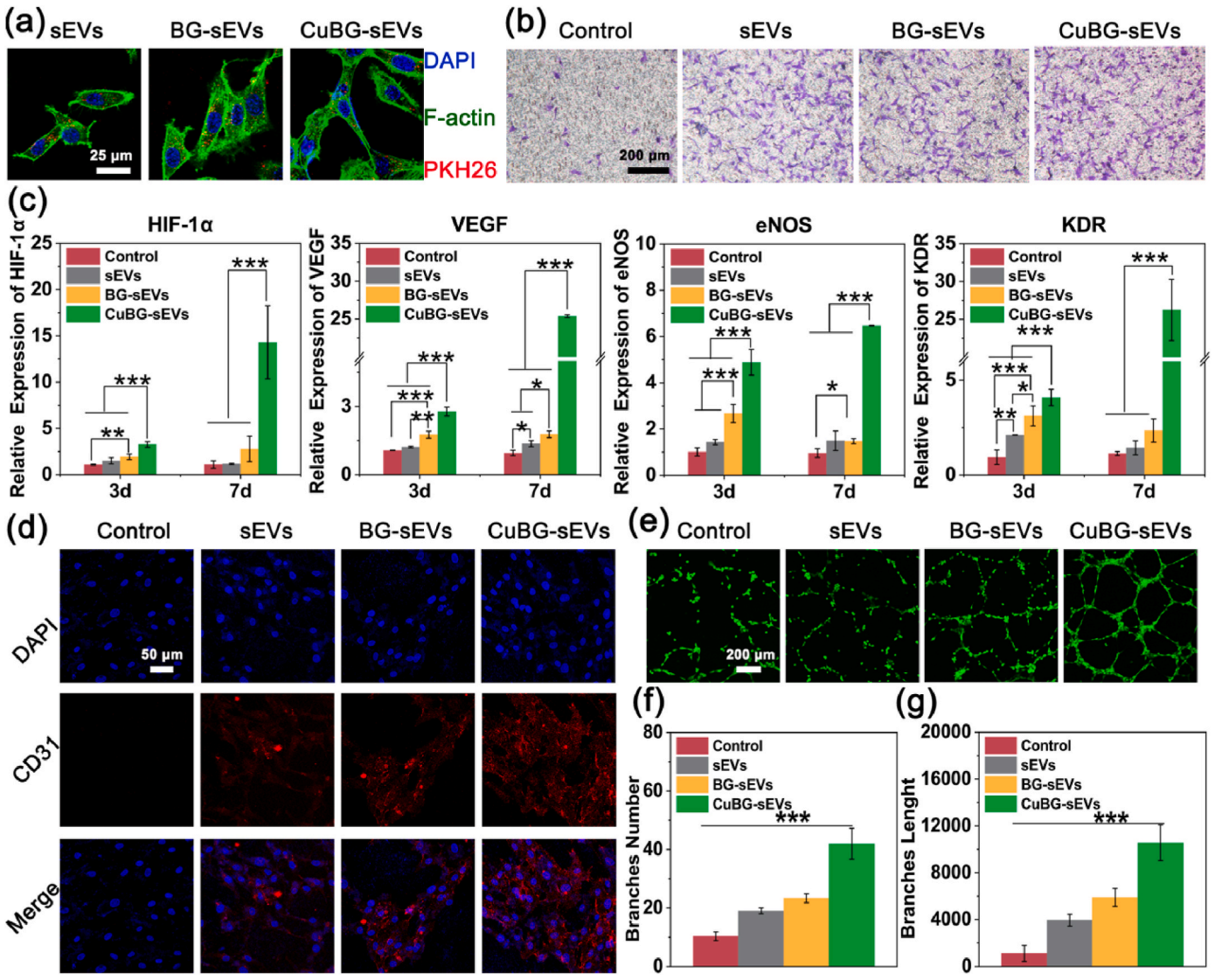

Fig. 4. Evaluation of CuBG-sEVs promoting angiogenesis in vitro. (a) Immunofluorescence staining of DAPI (blue), F-actin (green) and PKH26 (red). (b) Transwell staining. (c) Expression of angiogenesis-related genes, including HIF-1α, VEGF, eNOS, and KDR. (d) Immunofluorescence staining of CD31 (red) and DAPI (blue). (e) Calcein AM staining of matrigel matrix-forming vessels. (f) Number of branches in the matrigel vasculature assay. (g) Branches length of matrigel vasculature assay. n = 3, $^{*}p < 0.05$, $^{**}p < 0.01$, $^{***}p < 0.001$. Control, without sEVs; sEVs, untreated BMSCs-derived sEVs; BG-sEVs, BG treated BMSCs-derived sEVs. CuBG-sEVs, CuBG treated BMSCs-derived sEVs.

supported by the RT−qPCR results, which showed the up-regulation of important genes related to osteogenic regeneration, including ALP, RUNX2, OCN, BMP2, and COL1A1, after CuBG-sEVs treatment. Notably, the up-regulation of ALP and RUNX2 played a central role in the initial stages of bone matrix synthesis and mineralization. The miRNAs within CuBG-sEVs promoted the differentiation of BMSCs towards osteogenesis by modulating the osteogenesis-related signalling pathway Wnt/β-catenin, PI3K/Akt and MAPK signaling pathways [59,60]. The observation that miRNAs encapsulated within CuBG-sEVs regulated osteogenic differentiation targets further supported the idea that CuBG-sEVs could be an favorable alternative to CuBG.

2.4. Angiogenesis and osteogenesis in vivo

To exploit the potential of CuBG-sEVs for in vivo bone repair (Fig. 6a), tannin-coated gelatin methacryloyl croygel was served as a delivery platform for CuBG-sEVs, which exhibited avorable biocompatibility, mechanical properties and macroporous structure (Fig. 6b, Figs. S4a and S4b) [61,62]. Notably, the TG cryogel demonstrated exceptional sEVs adsorption capacity along with controlled release dynamics (Fig. 6c and d). SEM results confirmed the uniform adsorption of sEVs on the cryogel surface (Fig. S4c). Live/dead cell staining and MTT results indicated its biocompatibility (Figs. S5a and S5b). The ability of CuBG-sEVs/TG to stimulate new bone growth was evaluated in Sprague-Dawley (SD) rats using a critical skull defect model.

After 4 and 8 weeks of implantation, micro-CT was used to analyze 2D images of different cross-sections and 3D reconstructed images of all samples (Fig. 6e and S6). Compared to the control and TG groups, the CuBG-sEVs/TG group exhibited significantly more new bone formation at all time points, particularly at 8 weeks. The quantitative analysis of bone volume to total volume percentage (BV/TV) showed that the CuBG-sEVs/TG group showed a significantly higher value than the BG-sEVs/TG group (Fig. 6f–Table S1). At 8 weeks, the BV/TV for the CuBG-sEVs/TG group was 83.13 ± 2.21 %, which is 1.4 times that of the sEVs/TG group and 1.2 times that of the BG-sEVs group. Additionally, the bone regeneration quality in the CuBG-sEVs/TG group was significantly improved. At 8 weeks, the trabecular number (Tb.N) in the CuBG-sEVs/TG group was 2.5 times that of the control group, 1.7 times that of

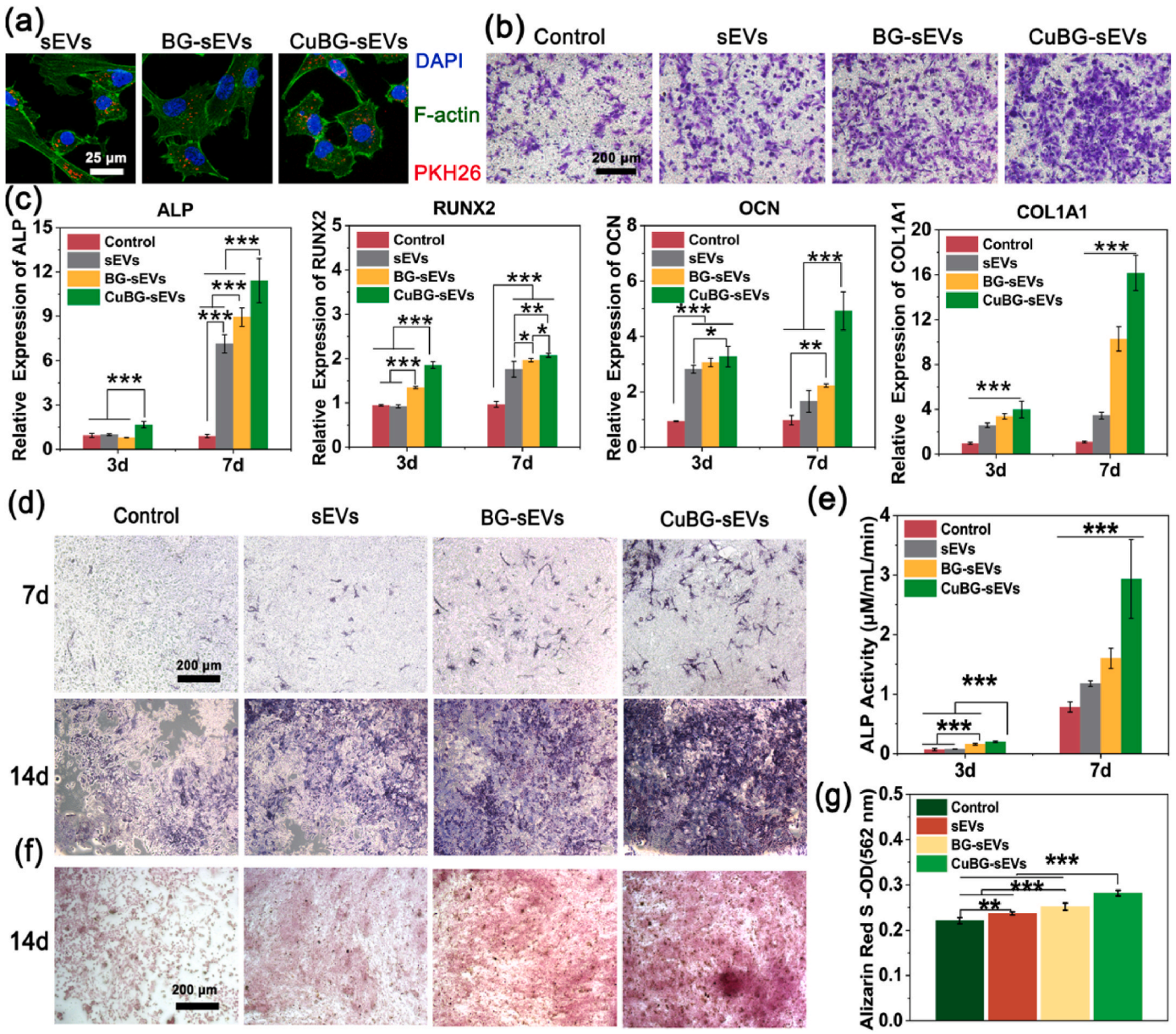

Fig. 5. Detection of the ability of CuBG-sEVs to induce osteogenesis in vitro. (a) Immunofluorescence staining of DAPI (blue), F-actin (green) and PKH26 (red). (b) Transwell staining of BMSCs. (c) Expression of osteogenesis genes, including ALP, RUNX2, OCN, and COL1A1. (d–e) ALP staining of BMSCs. (f–g) Alizarin red staining and quantitative data. n = 3, $^{*}p < 0.05$, $^{**}p < 0.01$, $^{***}p < 0.001$. Control, without sEVs; sEVs, untreated BMSCs-derived sEVs; BG-sEVs, BG treated BMSCs-derived sEVs. CuBG-sEVs, CuBG treated BMSCs-derived sEVs.

the sEVs/TG group, and 1.5 times that of the BG-sEVs group, all showing statistical significance (Fig. 6g). The trabecular thickness (Tb.Th) results at 4 and 8 weeks were consistent with the BV/TV and Tb.N results, with the CuBG-sEVs/TG group significantly higher than the other groups (Fig. 6h). Overall, these results indicated that the CuBG-sEVs/TG group showed significantly better bone repair in terms of both area and quality compared to the other groups.

To further evaluate the efficacy of CuBG-sEVs/TG in bone regeneration, hematoxylin and eosin (H&E) staining and masson staining were performed. The H&E staining results showed that, at 4 weeks, the CuBG-sEVs/TG group had significantly increased extracellular matrix deposition and smaller defect areas (blue dashed region) compared to the control and sEVs/TG groups, with a notable increase in new bone area (green triangles) (Fig. 7a). At 8 weeks, consistent with the micro-CT results, the control group only had minimal new bone regeneration. In comparison to the sEVs/TG group, the CuBG-sEVs/TG group showed a significant increase in extracellular matrix deposition, with the new bone at the defect edges tending to connect, indicating that the sustained release of highly active CuBG-sEVs promoted extracellular matrix deposition and accelerated bone healing. Furthermore, as shown in Fig. 7b, Masson staining results demonstrated that the control group had a smaller collagen regeneration area (blue dashed region). In contrast, the CuBG-sEVs/TG group exhibited significantly more collagen formation, with denser and more mature collagen fibers. The CuBG-sEVs/TG group showed continuous and substantial new bone formation at the defect margins, with new bone extending towards the center of the defect, which is not observed in the other groups.

Immunofluorescence staining was performed to investigate the interaction between angiogenesis and bone formation. At 4 weeks, both the sEVs/TG and BG-sEVs/TG groups exhibited increased CD31/α-SMA positive staining compared to the control and TG groups (Fig. 8a–d). Notably, the CuBG-sEVs/TG group exhibited the largest area of positive

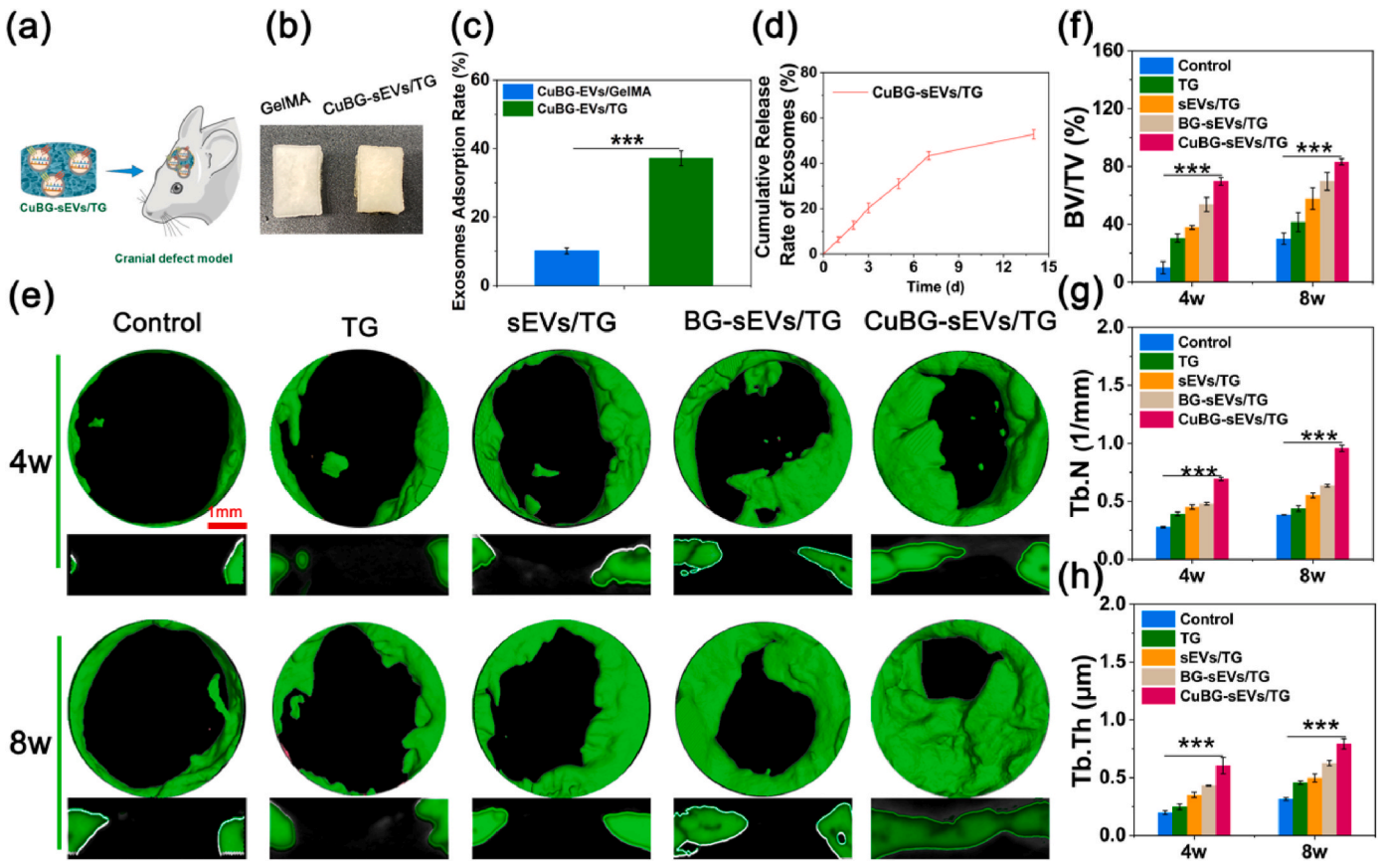

Fig. 6. CuBG-sEVs/TG promotes cranial bone repair in rats. (a) Scheme of CuBG-sEVs/TG applied to cranial bone defects in rats. (b) Photoes of the croygel. (c) Load efficiency of sEVs. (d) Release of sEVs from TG. (e) Micro-CT images of rat cranial bone regeneration. (f) Quantitative analyses of new bone area, BV/TV. (g) Quantitative analyses of new bone area,Tb.N. (h) Quantitative analyses of new bone area, Tb.Th. n = 3, $^{*}p < 0.05$, $^{**}p < 0.01$, $^{***}p < 0.001$. Control, without hydrogel; TG, hydrogel group; sEVs/TG, hydrogel group containing sEVs; BG-sEVs/TG, hydrogel group containing BG-sEVs; CuBG-sEVs/TG, hydrogel group containing CuBG-sEVs.

staining, which was 1.3 times that of the sEVs/TG group. Subsequently, the vascular network underwent progressive reconstruction and fusion, with the CuBG-sEVs/TG group attaining peak angiogenesis activity for 8 weeks. OCN immunofluorescence outcomes revealed substantial positive expression in the CuBG-sEVs/TG group with a 1.3-fold increase compared to sEVs/TG group (Fig. 8b–e). Moreover, COL I staining depicted (Fig. 8c–f) pronounced expression in the CuBG-sEVs. This heightened expression persisted for 8 weeks, which was 6.9 times that of the sEVs/TG group. From the results of immunofluorescence, it could be observed that osteogenesis and angiogenesis were highly coupled in time and space, indicating that CuBG-sEVs/TG group supported osteogenesis by promoting angiogenesis.

Angiogenesis played a critical role in supporting osteogenesis and ultimately determining the final bone regeneration. CD31 protein has been identified as an important component of angiogenesis [63]. Immunofluorescence staining showed a significant increase in CD31 expression within the CuBG-sEVs/TG group for 4 weeks, as indicated by broad positive staining. The CuBG-sEVs effectively harnessed miR-210 to orchestrate angiogenesis and regulate vascular function by upregulating VEGF expression through binding to KDR, concomitant with an elevation in eNOS expression, ultimately resulting in CD31 expression [64]. Augmented CD31 expression encouraged the adhesion and aggregation of HUVECs, bolstered angiogenesis and provided essential nutrients and oxygen to nascent bone tissue [65,66]. At 8 weeks, positive OCN staining was concentrated in the peripheral area of the defect, indicating ongoing osteogenesis [67]. It was noteworthy that miRNAs such as miR-218, miR-146a and miR-21, which were contained within CuBG-sEVs, enhanced OCN expression, thereby propelling osteogenic activity by activating signaling pathways relevant to osteogenesis [60,68]. Additionally, COL I, a pivotal constituent of the bone matrix, which is responsible for supporting and safeguarding new bone during the regeneration process [69]. Following 8 weeks of intervention with CuBG-sEVs/TG, COL I displayed a well ordered pattern and robust interlinking with endogenous new bone, functioning as a structural framework that facilitates cell migration and colonization. CuBG-sEVs facilitate angiogenesis, cellular recruitment and osteogenic differentiation, thereby enabling comprehensive regenerative repair of critical bone defects. Overall, CuBG-sEVs expedite bone regeneration by promoting angiogenesis, enhancing COL I deposition [11,13]. Subsequent investigations should examine the efficacy of our system in promoting bone regeneration during the initial stages of healing and explore the molecular mechanisms responsible for osteogenesis. For future clinical extension, extensive research is necessary to increase the number of experimental animals and investigate the impact of the properties of materials and pathological microenvironment in animals on the release and activity of sEVs. Additionally, a more comprehensive understanding of the mechanism by which CuBG-sEVs/TG promotes tissue regeneration in vivo is required.

3. Conclusion

In summary, a nano-vibration exciter, CuBG-sEVs, was engineered to effectively transduce the ion signal of CuBG into miRNA signal via the HIF signaling pathway. CuBG extracts increased the production of CuBG-sEVs and promoted enrichment of angiogenesis and osteogenesis related miRNAs through regulating the HIF-1 signaling pathway and

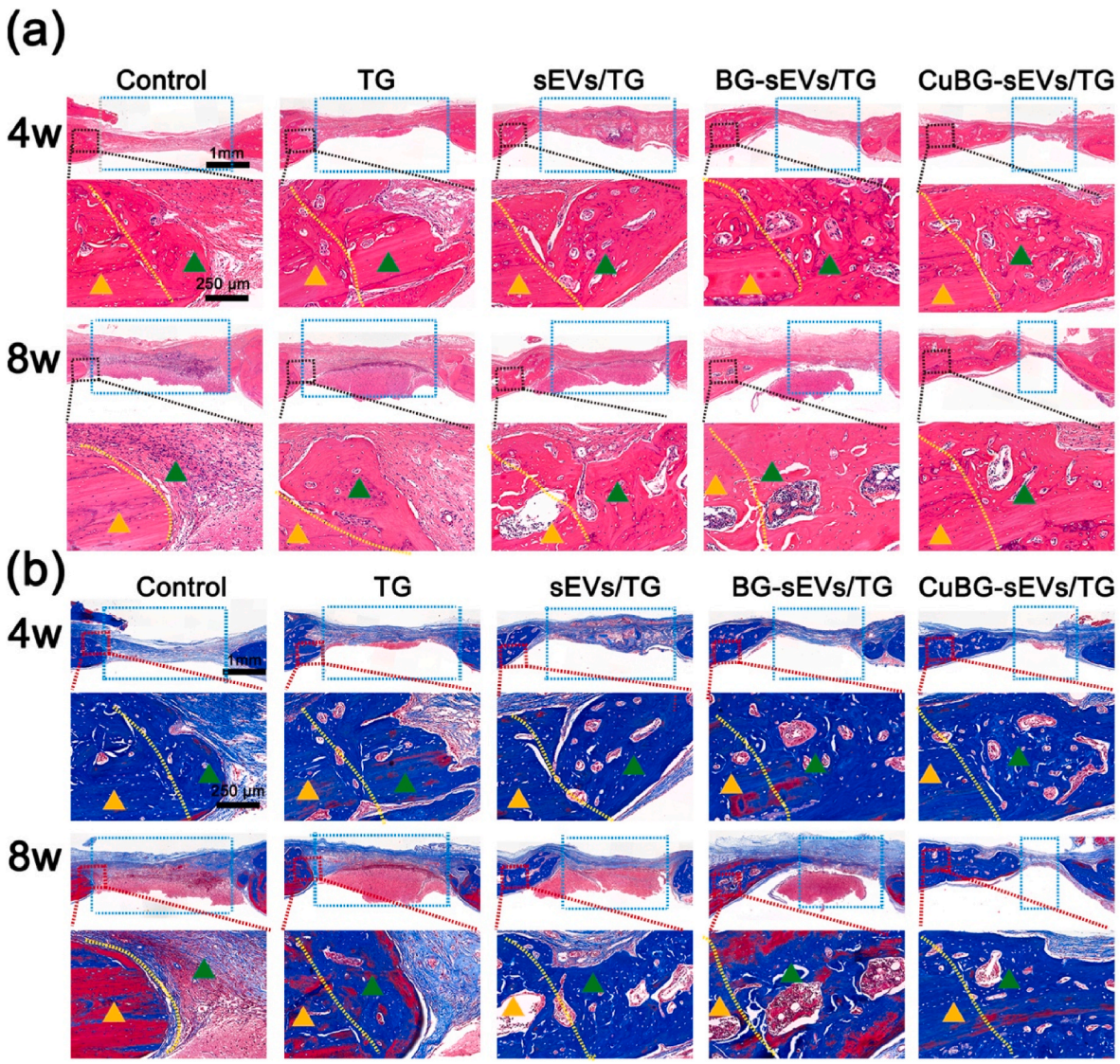

Fig. 7. (a) H&E staining. Vertical dashed lines indicate the areas of original defects. Green arrows indicate new bone tissues. Yellow arrows indicate native bones. Blue dashed areas indicate defective tissue. (b) Masson staining. Green arrows indicate new bone tissues. Yellow arrows indicate collagen matrix deposits. Blue dashed areas indicate defective tissue. Control, without hydrogel; TG, hydrogel group; sEVs/TG, hydrogel group containing sEVs; BG-sEVs/TG, hydrogel group containing BG-sEVs; CuBG-sEVs/TG, hydrogel group containing CuBG-sEVs.

activating autophagy process. Due to the enrichment of angiogenesis and osteogenesis-associated miRNAs, such as miR-210, miR-218, miR-146a and miR-21, CuBG-sEVs could be rapidly internalized by HUVECs and BMSCs, recruited cells, facilitated angiogenesis of HUVECs and osteogenic differentiation of BMSCs. Furthermore, the combination of CuBG-sEVs with TG cryogel resulted in remarkable bone regeneration in a critical bone defects model of rat. In conclusion, our findings proposed an attractive alternative strategy for BG in bone regeneration therapy.

4. Methods

4.1. Preparation of CuBG extracts

Based on previously reported methods, CuBG was prepared with a molar composition of $60SiO_2$–$34CaO$–$2CuO$–$4P_2O_5$ [11,13]. Briefly, 4 g of dodecylamine was measured and dissolved in a mixture of 20 mL of deionised water and 80 mL of ethanol, followed by the addition of 16 mL of tetraethyl orthosilicate (TEOS, Aladdin, China) and stirring at room temperature for 1 h. Then, 1.66 mL of triethyl phosphate (TEP, Aladdin, China), $Ca(NO_3)_2$–$4H_2O$, and $Cu(NO_3)_2$–$3H_2O$ (Aladdin, China) were added sequentially to the TEOS solution for further reaction. Further reaction. The reaction was carried out at room temperature with vigorous stirring for 4 h. After aging at room temperature for 1 d, the precipitates of different colours were collected by centrifugation and washing. BG and CuBG were obtained by sintering in air at 650 °C for 3 h. The precipitates were stored in a dry cabinet.

Then, 0.2 g/mL CuBG was added to the complete medium, which included dulbecco's modified eagle medium (DMEM, Solarbio, China), Fetal Bovine Serum (FBS, Tianhang, China) and penicillin streptomycin in classic proportions. The microstructure was observed by SEM (Zeiss, German), and the particle size distribution was analyzed using ImageJ, and analyzed using XRD (Empyrean, Netherlands) testing.

After incubation in a constant temperature shaker (37 °C, 120 rpm) for 24 h and centrifugation at 8000 rpm, the ion concentrations of the extracts were analyzed using inductively coupled plasma−optical emission spectrometry (ICP−OES, PerkinElmer PinAAcle 900 T, Germany). Finally, extracted of CuBG were obtained for cell culture. CCK8 (Beyotime, China) was tested and analyzed according to the manufacturer's instructions.

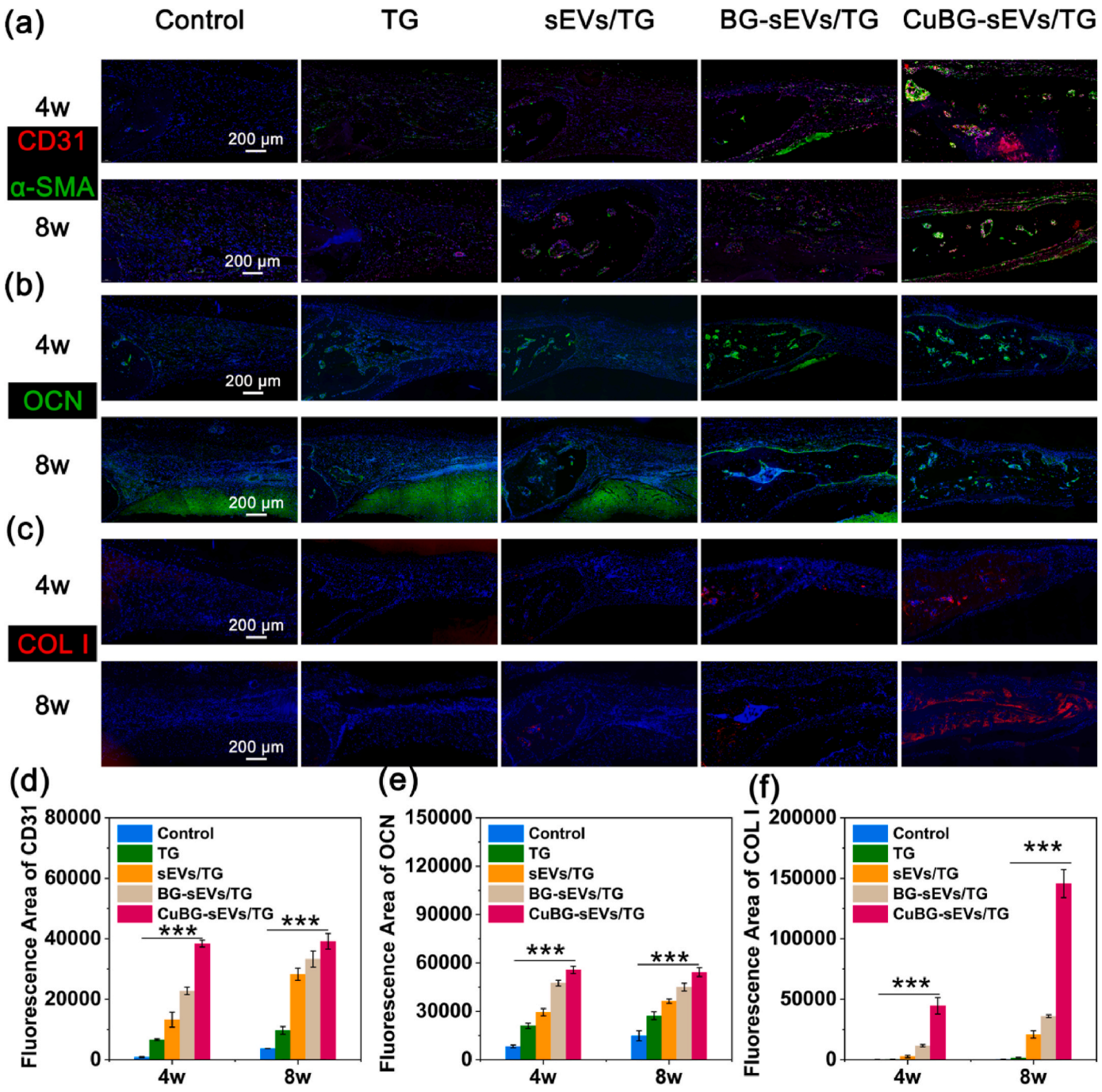

Fig. 8. Immunofluorescence staining of tissue sections. (a) Immunofluorescence staining for CD31/α-SMA protein; red indicates the CD31 protein, blue indicates the nucleus, and green indicates the α-SMA protein. (b) OCN protein staining; green indicates the OCN protein, and blue indicates the nucleus. (c) COL I protein staining; red indicates the COL I protein, and blue indicates the nucleus. (d) Quantitative results of immunofluorescence area of CD31. (e) Quantitative results of immunofluorescence area of OCN. (f) Quantitative results of immunofluorescence area of COL I. n = 3, $^{*}p < 0.05$, $^{**}p < 0.01$, $^{***}p < 0.001$. Control, without hydrogel; TG, hydrogel group; sEVs/TG, hydrogel group containing sEVs; BG-sEVs/TG, hydrogel group containing BG-sEVs; CuBG-sEVs/TG, hydrogel group containing CuBG-sEVs.

4.2. Extracts and characterization of sEVs

This study employed differential centrifugation to isolate sEVs [34, 70]. The procedure involved incubating BMSCs (2×10^6 cells, CRL-12424, American Type Culture Collection, America) with CuBG or BG extracts in DMEM (5 mL, free FBS) for 48 h. The resulting medium underwent successive centrifugations at 2000×*g* and 10,000×*g* for 30 min to eliminate larger particles such as cells and apoptotic debris. The collected supernatant then underwent final centrifugation at 100,000×*g* for 70 min to pellet the sEVs. These sEVs were subsequently resuspended and washed with phosphate buffered saline (PBS) twice, and the resulting solution was filtered through a 0.22 μm sterile filter. The protein concentration of the sEVs was assessed using the BCA Protein Assay Kit (Solarbio, China). TEM (HT7700, HITACHI, Japan) was used to visualize the morphology. The particle size distribution was determined through zeta potential analysis (Malvern, America). The presence of related proteins (CD9, CD63, calnexin, LC3B, p62, Bioss) was verified using Western blotting.

4.3. Cellular uptake with transwell assays

To visualize sEVs, PHK26 staining (Sigma–Aldrich, America) was used. Subsequently, these labeled sEVs (10 μg/mL) were introduced to BMSCs cultured in laser confocal dishes at a density of 1×10^5 cells/well for a 24 h incubation. After fixation with 4 % paraformaldehyde for 20 min, DAPI (Beyotime, China) and F-actin (Beyotime, China) staining were conducted. Images were captured and assessed using laser confocal microscopy (LSCM, TCS SP8, Leica, Germany).

For the Transwell assay, BMSCs were seeded in the upper chamber at a concentration of 1×10^5 cells/well, while the lower chamber was exposed to 600 μL of sEVs for 12 h. Following fixation with 4 % paraformaldehyde for 20 min, crystal violet (0.1 %) staining was performed for 30 min. Subsequent photographic documentation and analysis were performed using an inverted microscope and ImageJ software.

4.4. Gene expression

Total RNA was extracted using the Total RNA Kit I (Omega, America) and then converted into cDNA using a reverse transcription kit (Takara, Japan). RT–qPCR was conducted using LightCycler 480 SYBR Green I Master (Roche, Switzerland) and analyzed using LightCycler® 480II (Roche, Switzerland). The quantification was performed using the $2^{-\Delta\Delta Ct}$ method. The primers for each gene were listed in Table S2.

4.5. Immunofluorescence analysis

BMSCs were cultured for 24 h in laser confocal dishes at a density of 1×10^5 cells/well. Following this, coculture with sEVs was performed for an additional 24 h. For fixation, 4 % paraformaldehyde was applied for 20 min. Subsequently, cell membrane permeability was achieved by using 0.2 % Triton X-100 for 10 min, followed by blocking with goat serum (3 %) for 30 min. Primary antibodies (CD63, CD31, HIF-1α, Bioss) were then introduced and allowed to incubate overnight at 4 °C. Sequentially, the secondary antibody treatment was carried out at room temperature for 2 h while avoiding any light exposure. Finally, DAPI staining was performed for 5 min to label the nuclei. The images were captured and analyzed using LSCM.

4.6. Analysis of matrigel matrix vasculogenesis

The tip was precooled to 4 °C before applying 50 μL of matrigel matrix (Beyotime, China) to coat the interior of 96-well plates. This process was performed under chilled conditions. Afterward, the well plates were transferred to an incubator, allowing the matrix gel to solidify completely within 2 h. After the gel solidified, a cell density of 5×10^4 cells/well was used. HUVECs (DFSC-EC-01, Shanghai Zhong Qiao Xin Zhou Biotechnology Co.,Ltd, China) were inoculated into the well plates and incubated at 37 °C for 8 h (third generation). At the conclusion of the incubation period, calcein AM (1 mg/mL, 15 min, Beyotime, China) was introduced for cell staining. Subsequently, image acquisition and recording were executed using an inverted fluorescence microscope. Finally, ImageJ software (angiogenesis analyze plug-in) was used for quantitative analysis of the angiogenesis process, including the determination of vascular branching and length [71].

4.7. Alizarin red staining and alkaline phosphatase staining

The ability of CuBG-sEVs to promote osteogenesis was evaluated using BMSCs (1×10^5 cells/well). First, BMSCs were seeded in 24-well plates and cultured for 24 h. Then, the medium was replaced with fresh medium containing CuBG-sEVs. After being cultured in different kinds of cell medium for 7 and 14 days, BMSCs (1×10^5 cells/well) were first fixed in 4 % paraformaldehyde for 20 min and then washed gently with PBS. Alizarin red staining solution (2 %) (Beyotime, China) was used for staining, and the stained samples were imaged using an inverted fluorescence microscope. Following the same pretreatment as ARS staining, a BCIP/NBT Alkaline Phosphatase Color Development Kit (Beyotime, China) was used to stain BMSCs for 30 min. The stained samples were then imaged using an inverted fluorescence microscope.

4.8. Preparation of GelMA cryogel

GelMA was synthesized according to established protocols and subsequently analyzed using FTIR (Nexus Por Euro, America) spectroscopy, with a degree of methacryloyl (MA) substitution of about to be 90 % [72]. The preparation of the GelMA cryogel followed a well-documented procedure. Initially, 2 g of GelMA was solubilized in 20 mL of PBS at 40 °C while being stirred for 30 min. The GelMA solution was then compounded individually with the needed components, along with 0.5 % (w/v) ammonium persulfate (APS, Sigma–Aldrich, America) and 0.5 % (v/v) tetramethylethylenediamine (TEMED, Sigma–Aldrich, America). Following vigorous stirring for 5 min, the mixture was poured into molds and stored at −20 °C for 36 h, followed by freeze drying to obtain the final samples.

4.9. Loading and release of sEVs

CuBG-sEVs/TG cryogels were prepared using a systematic procedure. Initially, the GelMA cryogel was submerged in a 0.2 mg/mL TA solution for 15 min and then washed with PBS three times. The TG were then immersed in a solution containing CuBG-sEVs (500 μg/mL) and gently stirred at low temperature for 2 h, forming CuBG-sEVs/TG scaffolds. To facilitate the controlled release of sEVs, the hydrogels were incubated in 5 mL of PBS at 37 °C. At specified time intervals, 200 μL of the solution was withdrawn and replaced with an equal volume of PBS. The quantification of sEVs was achieved using the BCA Protein Assay Kit, which allowed for the determination of the released amount. The microscopic characteristics of the CuBG-sEVs/TG cryogel were examined using SEM.

4.10. Biocompatibility of TG

The biocompatibility of the scaffolds was assessed using a combination of MTT assay and live/dead cell staining. Initially, BMSCs at a density of 1×10^5 cells/well were seeded onto the scaffold surfaces and cultured for 1, 3 and 7 days. The MTT assay was executed as per the manufacturer's protocol from the MTT assay kit (Solarbio, China), followed by absorbance measurement at 570 nm using an enzyme marker. Live/dead cell staining was carried out using calcein AM/propidium iodide (calcein AM/PI, Beyotime, China), and subsequent image acquisition and analysis were performed using LSCM.

4.11. Calvarial defect model

The animal experiments were conducted in accordance with the ethical guidelines of the Animal Ethics Committee at South China University of Technology (2019005). Initially, 30 male SD rats aged 8 weeks and weighing between 200 and 250 g were chosen for the study. Anesthesia was induced using a 0.3 % solution of pentobarbital, followed by a 1 cm incision on their heads. Subsequently, a defect with a diameter of 0.5 cm was meticulously created in the skull using a ring drill, ensuring the protection of the dura mater to prevent any accidental damage. A material measuring (diameter × 5 mm, height × 1 mm) was then implanted into the defect site and sutured. After surgery, the rats were returned to the animal housing facility and allowed to move around freely. Continuous penicillin injections were administered for three days to prevent infections.

4.12. Histological analysis

For 4 and 8 weeks, humane euthanasia was performed on SD rats,

and their skull specimens were carefully excised. The specimens were then detected using micro-CT scanning (XTV 160, Nikon, Japan) for thorough examination. The harvested tissues were immersed in 4 % paraformaldehyde for 72 h, followed by a series of procedures, including decalcification, embedding, and sectioning. Subsequently, the sections underwent staining techniques such as H&E and Masson staining (Solarbio, China), as well as immunofluorescence staining (CD31, OCN, COL I, α-SMA, Bioss) individually. A digital pathology scanning system (P250 FLASH, 3D Histech, Hungary) was used to capture and analyze the images.

4.13. Statistical analysis

Using SPSS 22.0 statistical analysis software, a one-way analysis of variance followed by Tukey's test for means comparison was used to assess the level of significance.

Ethics approval and consent to participate

The animal experiments were conducted in accordance with the ethical guidelines of the Animal Ethics Committee at South China University of Technology (2019005).

CRediT authorship contribution statement

Zetao Wang: Writing – review & editing, Writing – original draft, Methodology, Formal analysis, Data curation, Conceptualization. **Qiyuan Dai:** Supervision, Project administration, Methodology, Data curation, Conceptualization. **Huitong Luo:** Validation. **Xiyuan Han:** Methodology. **Qi Feng:** Software, Project administration, Methodology. **Xiaodong Cao:** Writing – review & editing, Writing – original draft, Resources, Funding acquisition.

Declaration of competing interest

The authors declare that they have no known competing financial interests or personal relationships that could have appeared to influence the work reported in this paper.

Acknowledgments

This work was supported by the National Key R&D Program of China (2023YFB3810200), the National Natural Science Foundation of China (Grant No. 52272276, 52073103, 52203164), the Fundamental Research Funds for the Central Universities (No. 2022ZYGXZR105), the Project funded by China Postdoctoral Science Foundation (No. 2022M711183), the Science and Technology Planning Project of Guangzhou (2023A04J0971).

Appendix A. Supplementary data

Supplementary data to this article can be found online at https://doi.org/10.1016/j.bioactmat.2024.06.023.

References

[1] M. Liu, X. Zeng, C. Ma, H. Yi, Z. Ali, X.B. Mou, S. Li, Y. Deng, N.Y. He, Injectable hydrogels for cartilage and bone tissue engineering, Bone Res 5 (2017) 20. https://10.1038/boneres.2017.14.

[2] J. Qu, X. Zhao, Y.P. Liang, T.L. Zhang, P.X. Ma, B.L. Guo, Antibacterial adhesive injectable hydrogels with rapid self-healing, extensibility and compressibility as wound dressing for joints skin wound healing, Biomaterials 183 (2018) 185–199. https://10.1016/j.biomaterials.2018.08.044.

[3] H.W. Kang, S.J. Lee, I.K. Ko, C. Kengla, J.J. Yoo, A. Atala, A 3D bioprinting system to produce human-scale tissue constructs with structural integrity, Nat. Biotechnol. 34 (3) (2016) 312–319. https://10.1038/nbt.3413.

[4] D. Orlic, J. Kajstura, S. Chimenti, I. Jakoniuk, S.M. Anderson, B.S. Li, J. Pickel, R. McKay, B. Nadal-Ginard, D.M. Bodine, A. Leri, P. Anversa, Bone marrow cells regenerate infarcted myocardium, Nature 410 (6829) (2001) 701–705. https://10.1038/35070587.

[5] R. Zhao, W. Tang, F. Yang, H. Tian, S. Peng, H. Pan, C. Shuai, Structural and functional adaptive artificial bone: materials, fabrications, and properties, Adv. Funct. Mater. 33 (23) (2024) 2214726. https://doi.org/10.1002/adfm.202214726.

[6] A Brunet, MA Goodell, T Rando, Ageing and rejuvenation of tissue stem cells and their niches, Nat. Rev. Mol. Cell Biol. 24 (1) (2023) 45–62. https://10.1038/s41580-022-00510-w.

[7] A. Hoppe, N.S. Guldal, A.R. Boccaccini, A review of the biological response to ionic dissolution products from bioactive glasses and glass-ceramics, Biomaterials 32 (11) (2011) 2757–2774. https://10.1016/j.biomaterials.2011.01.004.

[8] G. Kaur, O.P. Pandey, K. Singh, D. Homa, B. Scott, G. Pickrell, A review of bioactive glasses: their structure, properties, fabrication, and apatite formation, J. Biomed. Mater. Res., Part A 102 (1) (2014) 254–274. https://10.1002/jbm.a.34690.

[9] A. Jacobs, G. Renaudin, C. Forestier, J.M. Nedelec, S. Descamps, Biological properties of copper-doped biomaterials for orthopedic applications: a review of antibacterial, angiogenic and osteogenic aspects, Acta Biomater. 117 (2020) 21–39. https://10.1016/j.actbio.2020.09.044.

[10] J.Y. Li, D. Zhai, F. Lv, Q.Q. Yu, H.S. Ma, J.B. Yin, Z.F. Yi, M.Y. Liu, J. Chang, C. T. Wu, Preparation of copper-containing bioactive glass/eggshell membrane nanocomposites for improving angiogenesis, antibacterial activity and wound healing, Acta Biomater. 36 (2016) 254–266. https://10.1016/j.actbio.2016.03.011.

[11] Q. Dai, Q. Li, H. Gao, L. Yao, Z. Lin, D. Li, S. Zhu, C. Liu, Z. Yang, G. Wang, D. Chen, X. Chen, X. Cao, 3D printing of Cu-doped bioactive glass composite scaffolds promotes bone regeneration through activating the HIF-1α and TNF-α pathway of hUVECs, Biomater Sci-Uk 9 (16) (2021) 5519–5532. https://10.1039/d1bm00870f.

[12] S. Kargozar, M. Mozafari, S. Ghodrat, E. Fiume, F. Baino, Copper-containing bioactive glasses and glass-ceramics: from tissue regeneration to cancer therapeutic strategies, Mat Sci Eng C-Mater 121 (2021) 18. https://10.1016/j.msec.2020.111741.

[13] Y.W. Liu, G. Wang, H.T. Luo, B.J. Zhao, M.H. Liao, Q.Y. Dai, M.C. Li, Q.T. Li, X. D. Cao, Phosphoserine enhanced Cu-doped bioactive glass dynamic dual-network hydrogel for craniofacial bone defect repair, Regen. Biomater. 10 (2023) 14. https://10.1093/rb/rbad054.

[14] C.T. Wu, Y.H. Zhou, M.C. Xu, P.P. Han, L. Chen, J. Chang, Y. Xiao, Copper-containing mesoporous bioactive glass scaffolds with multifunctional properties of angiogenesis capacity, osteostimulation and antibacterial activity, Biomaterials 34 (2) (2013) 422–433. https://10.1016/j.biomaterials.2012.09.066.

[15] W.J. Zhang, Q. Chang, L. Xu, G.L. Li, G.Z. Yang, X. Ding, X.S. Wang, D.X. Cui, X. Q. Jiang, Graphene oxide-copper nanocomposite-coated porous CaP scaffold for vascularized bone regeneration via activation of hif-1, Adv. Healthcare Mater. 5 (11) (2016) 1299–1309. https://10.1002/adhm.201500824.

[16] J.J. Wu, K. Zheng, X.T. Huang, J.Y. Liu, H.M. Liu, A.R. Boccaccini, Y. Wan, X. D. Guo, Z.W. Shao, Thermally triggered injectable chitosan/silk fibroin/bioactive glass nanoparticle hydrogels for in-situ bone formation in rat calvarial bone defects, Acta Biomater. 91 (2019) 60–71. https://10.1016/j.actbio.2019.04.023.

[17] M.H. Liao, S.L. Zhu, A.J. Guo, X.Y. Han, Q.T. Li, Y. Chen, Y.W. Liu, D.F. Chen, X. F. Chen, S.X. Mo, X.D. Cao, 3D printed bioactive glasses porous scaffolds with high strength for the repair of long-bone segmental defects, Compos. Pt. B-Eng. 254 (2023) 15. https://10.1016/j.compositesb.2023.110582.

[18] G. Raposo, W. Stoorvogel, Extracellular vesicles: exosomes, microvesicles, and friends, JCB (J. Cell Biol.) 200 (4) (2013) 373–383. https://10.1083/jcb.201211138.

[19] J.B. Fan, C.S. Lee, S. Kim, C. Chen, T. Aghaloo, M. Lee, Generation of small RNA-modulated exosome mimetics for bone regeneration, ACS Nano 14 (9) (2020) 11973–11984. https://10.1021/acsnano.0c05122.

[20] R. Kalluri, V.S. LeBleu, The biology, function, and biomedical applications of exosomes, Science 367 (6478) (2020) 640. https://10.1126/science.aau6977.

[21] L. Fan, C. Liu, X. Chen, L. Zheng, Y. Zou, H. Wen, P. Guan, F. Lu, Y. Luo, G. Tan, P. Yu, D. Chen, C. Deng, Y. Sun, L. Zhou, C. Ning, Exosomes-Loaded electroconductive hydrogel synergistically promotes tissue repair after spinal cord injury via immunoregulation and enhancement of myelinated axon growth, Adv. Sci. 9 (13) (2022) e2105586. https://10.1002/advs.202105586.

[22] H. Valadi, K. Ekström, A. Bossios, M. Sjöstrand, J.J. Lee, J.O. Lötvall, Exosome-mediated transfer of mRNAs and microRNAs is a novel mechanism of genetic exchange between cells, Nat. Cell Biol. 9 (6) (2007) 654–659. https://10.1038/ncb1596.

[23] K. O'Brien, K. Breyne, S. Ughetto, L.C. Laurent, X.O. Breakefield, RNA delivery by extracellular vesicles in mammalian cells and its applications, Nat. Rev. Mol. Cell Biol. 21 (10) (2020) 585–606. https://10.1038/s41580-020-0251-y.

[24] Y. Zhuang, M.J. Cheng, M. Li, J.J. Cui, J.Y. Huang, C.L. Zhang, J.W. Si, K.L. Lin, H. B. Yu, Small extracellular vesicles derived from hypoxic mesenchymal stem cells promote vascularized bone regeneration through the miR-210-3p/EFNA3/PI3K pathway, Acta Biomater. 150 (2022) 413–426. https://10.1016/j.actbio.2022.07.015.

[25] B.D. Tong, Z.W. Liao, H. Liu, W.C. Ke, C.C. Lei, W.F. Zhang, H.Z. Liang, H.C. Wang, Y.Q. He, J. Lei, K.W. Yang, X.G. Zhang, G.C. Li, L. Ma, Y. Song, W.B. Hua, X. B. Feng, K. Wang, X.H. Wu, L. Tan, Y. Gao, C. Yang, Augmenting intracellular cargo delivery of extracellular vesicles in hypoxic tissues through inhibiting hypoxia-induced endocytic recycling, ACS Nano (2023) 2537–2553. https://10.1021/acsnano.2c10351.

[26] L.M. Li, J.F. Mu, Y. Zhang, C.Y. Zhang, T. Ma, L. Chen, T.C. Huang, J.H. Wu, J. Cao, S.Q. Feng, Y.Z. Cai, M. Han, J.Q. Gao, Stimulation by exosomes from hypoxia preconditioned human umbilical vein endothelial cells facilitates mesenchymal

stem cells angiogenic function for spinal cord repair, ACS Nano 16 (7) (2022) 10811–10823. https://10.1021/acsnano.2c02898.
[27] Y.M. Yang, Y.N. Wu, D.H. Yang, S.H. Neo, N.D. Kadir, D. Goh, J.X. Tan, V. Denslin, E.H. Lee, Z. Yang, Secretive derived from hypoxia preconditioned mesenchymal stem cells promote cartilage regeneration and mitigate joint inflammation via extracellular vesicles, Bioact. Mater. 27 (2023) 98–112. https://10.1016/j.bioactmat.2023.03.017.
[28] H.P. Wang, H. Flach, M. Onizawa, L. Wei, M.T. McManus, A. Weiss, Negative regulation of Hif1α expression and TH17 differentiation by the hypoxia-regulated microRNA miR-210, Nat. Immunol. 15 (4) (2014) 393–401. https://10.1038/ni.2846.
[29] P. Prasad, C.R. Gordijo, A.Z. Abbasi, A. Maeda, A. Ip, A.M. Rauth, R.S. DaCosta, X. Y. Wu, Multifunctional albumin–MnO_2 nanoparticles modulate solid tumor microenvironment by attenuating hypoxia, acidosis, vascular endothelial growth factor and enhance radiation response, ACS Nano 8 (4) (2014) 3202–3212. https://10.1021/nn405773r.
[30] C.T. Wu, Y.H. Zhou, W. Fan, P.P. Han, J. Chang, J. Yuen, M.L. Zhang, Y. Xiao, Hypoxia-mimicking mesoporous bioactive glass scaffolds with controllable cobalt ion release for bone tissue engineering, Biomaterials 33 (7) (2012) 2076–2085. https://10.1016/j.biomaterials.2011.11.042.
[31] M. Eldh, J. Lötvall, C. Malmhäll, K. Ekström, Importance of RNA isolation methods for analysis of exosomal RNA: evaluation of different methods, Mol. Immunol. 50 (4) (2012) 278–286. https://10.1016/j.molimm.2012.02.001.
[32] C. Stähli, M. James-Bhasin, A. Hoppe, A.R. Boccaccini, S.N. Nazhat, Effect of ion release from Cu-doped 45S5 Bioglass® on 3D endothelial cell morphogenesis, Acta Biomater. 19 (2015) 15–22. https://10.1016/j.actbio.2015.03.009.
[33] Q.Y. Dai, Q.T. Li, H.C. Gao, L.T. Yao, Z.F. Lin, D.G. Li, S.L. Zhu, C. Liu, Z. Yang, G. Wang, D.F. Chen, X.F. Chen, X.D. Cao, 3D printing of Cu-doped bioactive glass composite scaffolds promotes bone regeneration through activating the HIF-1α and TNF-α pathway of hUVECs, Biomater Sci-Uk 9 (16) (2021) 5519–5532. https://10.1039/d1bm00870f.
[34] Z.T. Wang, H.T. Luo, Z.Y. Zhou, Z.Y. He, S.L. Zhu, D.G. Li, H.C. Gao, X.D. Cao, Engineered multifunctional Silk fibroin cryogel loaded with exosomes to promote the regeneration of annulus fibrosus, Appl. Mater. Today 29 (2022) 13. https://10.1016/j.apmt.2022.101632.
[35] M. Zhang, W.H. Hu, C.H. Cai, Y. Wu, J.M. Li, S.W. Dong, Advanced application of stimuli-responsive drug delivery system for inflammatory arthritis treatment, Mater. Today Bio 14 (2022) 18. https://10.1016/j.mtbio.2022.100223.
[36] S.C. Tao, S.C. Guo, C.Q. Zhang, Modularized extracellular vesicles: the dawn of prospective personalized and precision medicine, Adv. Sci. 5 (2) (2018) 1700449. https://10.1002/advs.201700449.
[37] H.X. Zhang, J. Wu, J.H. Wu, Q. Fan, J.C. Zhou, J.W. Wu, S.C. Liu, J. Zang, J.H. Ye, M. Xiao, T. Tian, J. Gao, Exosome-mediated targeted delivery of miR-210 for angiogenic therapy after cerebral ischemia in mice, J. Nanobiotechnol. 17 (1) (2019) 29. https://10.1186/s12951-019-0461-7.
[38] N.M. Alajez, M. Lenarduzzi, E. Ito, A.B.Y. Hui, W. Shi, J. Bruce, S.J. Yue, S. H. Huang, W. Xu, J. Waldron, B. O'Sullivan, F.F. Liu, MiR-218 suppresses nasopharyngeal cancer progression through downregulation of survivin and the SLIT2-ROBO1 pathway, Cancer Res. 71 (6) (2011) 2381–2391. https://10.1158/0008-5472.Can-10-2754.
[39] L. Liu, F. Yu, L. Li, L.X. Zhou, T. Zhou, Y.J. Xu, K.L. Lin, B. Fang, L.G. Xia, Bone marrow stromal cells stimulated by strontium-substituted calcium silicate ceramics: release of exosomal miR-146a regulates osteogenesis and angiogenesis, Acta Biomater. 119 (1) (2021) 444–457. https://10.1016/j.actbio.2020.10.038.
[40] Z. Geng, X.G. Wang, J. Zhao, Z.Y. Li, L.L. Ma, S.L. Zhu, Y.Q. Liang, Z.D. Cui, H. Y. He, X.J. Yang, The synergistic effect of strontium-substituted hydroxyapatite and microRNA-21 on improving bone remodeling and osseointegration, Biomater Sci-Uk 6 (10) (2018) 2694–2703. https://10.1039/c8bm00716k.
[41] Y.K. Gao, Z.Y. Yuan, X.J. Yuan, Z. Wan, Y.J. Yu, Q. Zhan, Y.M. Zhao, J.M. Han, J. Y. Huang, C.Y. Xiong, Q. Cai, Bioinspired porous microspheres for sustained hypoxic exosomes release and vascularized bone regeneration, Bioact. Mater. 14 (2022) 377–388. https://10.1016/j.bioactmat.2022.01.041.
[42] G.L. Semenza, Targeting HIF-1 for cancer therapy, Nat. Rev. Cancer 3 (10) (2003) 721–732. https://10.1038/nrc1187.
[43] J. Kim, H.Y. Kim, S.Y. Song, S.H. Go, H.S. Sohn, S. Baik, M. Soh, K. Kim, D. Kim, H. C. Kim, N. Lee, B.S. Kim, T. Hyeon, Synergistic oxygen generation and reactive oxygen species scavenging by manganese ferrite/ceria Co-decorated nanoparticles for rheumatoid arthritis treatment, ACS Nano 13 (3) (2019) 3206–3217. https://10.1021/acsnano.8b08785.
[44] G.N. Masoud, W. Li, HIF-1α pathway: role, regulation and intervention for cancer therapy, Acta Pharm. Sin. B 5 (5) (2015) 378–389. https://10.1016/j.apsb.2015.05.007.
[45] U Berchner-Pfannschmidt, S Tug, M Kirsch, J Fandrey, Oxygen-sensing under the influence of nitric oxide, Cell Signal. 22 (3) (2010) 349–356. https://doi.org/10.1016/j.cellsig.2009.10.004.
[46] J. Cosin-Roger, S. Simmen, H. Melhem, K. Atrott, I. Frey-Wagner, M. Hausmann, C. de Vallière, M.R. Spalinger, P. Spielmann, R.H. Wenger, J. Zeitz, S.R. Vavricka, G. Rogler, P.A. Ruiz, Hypoxia ameliorates intestinal inflammation through NLRP3/mTOR downregulation and autophagy activation, Nat. Commun. 8 (1) (2017) 98. https://10.1038/s41467-017-00213-3.
[47] N Rohwer, T Cramer, Hypoxia-mediated drug resistance: novel insights on the functional interaction of HIFs and cell death pathways, Drug Resist. Updat. 14 (3) (2011) 191–201. https://10.1016/j.drup.2011.03.001.
[48] K. Qureshi-Baig, D. Kuhn, E. Viry, V.I. Pozdeev, M. Schmitz, F. Rodriguez, P. Ullmann, E. Koncina, M. Nurmik, S. Frasquilho, P.V. Nazarov, N. Zuegel, M. Boulmont, Y. Karapetyan, L. Antunes, D. Val, M. Mittelbronn, B. Janji, S. Haan, E. Letellier, Hypoxia-induced autophagy drives colorectal cancer initiation and progression by activating the PRKC/PKC-EZR (ezrin) pathway, Autophagy 16 (8) (2020) 1436–1452. https://10.1080/15548627.2019.1687213.
[49] Y. Kabeya, N. Mizushima, T. Uero, A. Yamamoto, T. Kirisako, T. Noda, E. Kominami, Y. Ohsumi, T. Yoshimori, LC3, a mammalian homologue of yeast Apg8p, is localized in autophagosome membranes after processing, EMBO J. 19 (21) (2000) 5720–5728. https://10.1093/emboj/19.21.5720.
[50] R.A. Saxton, D.M. Sabatini, mTOR signaling in growth, metabolism, and disease, Cell 168 (6) (2017) 960–976. https://10.1016/j.cell.2017.02.004.
[51] Z.W. Liao, S. Li, S.D. Lu, H. Liu, G.C. Li, L. Ma, R.J. Luo, W.C. Ke, B.J. Wang, Q. Xiang, Y. Song, X.B. Feng, Y.K. Zhang, X.H. Wu, W.B. Hua, C. Yang, Metformin facilitates mesenchymal stem cell-derived extracellular nanovesicles release and optimizes therapeutic efficacy in intervertebral disc degeneration, Biomaterials 274 (2021) 16. https://10.1016/j.biomaterials.2021.120850.
[52] A.J. van Wijnen, J. van de Peppel, J.P. van Leeuwen, J.B. Lian, G.S. Stein, J. J. Westendorf, M.J. Oursler, H.J. Im, H. Taipaleenmaki, E. Hesse, S. Riester, S. Kakar, MicroRNA functions in osteogenesis and dysfunctions in osteoporosis, Curr. Osteoporos. Rep. 11 (2) (2013) 72–82. https://10.1007/s11914-013-0143-6.
[53] H. Feng, Z.Y. Li, W.J. Xie, Q.B. Wan, Y.W. Guo, J.Y. Chen, J. Wang, X.B. Pei, Delivery of therapeutic miRNAs using nanoscale zeolitic imidazolate framework for accelerating vascularized bone regeneration, Chem. Eng. J. 430 (2022) 11. https://10.1016/j.cej.2021.132867.
[54] M. Grunewald, I. Avraham, Y. Dor, E. Bachar-Lustig, A. Itin, S. Yung, S. Chimenti, L. Landsman, R. Abramovitch, E. Keshet, VEGF-induced adult neovascularization: recruitment, retention, and role of accessory cells, Cell 124 (1) (2006) 175–189. https://10.1016/j.cell.2005.10.036.
[55] N. Ferrara, H.P. Gerber, J. LeCouter, The biology of VEGF and its receptors, Nat. Med. 9 (6) (2003) 669–676. https://10.1038/nm0603-669.
[56] M.D. Li, P.L. Wang, S.T. Huo, H. Qiu, C.D. Li, S.Y. Lin, L.B. Guo, Y.C. Ji, Y.L. Zhu, J. Y. Liu, J.Y. Guo, J. Na, Y.T. Hu, Human pluripotent stem cells derived endothelial cells repair choroidal ischemia, Adv. Sci. (2023) 17. https://10.1002/advs.202302940.
[57] H.G. Cui, M.J. Webber, S.I. Stupp, Self-assembly of peptide amphiphiles: from molecules to nanostructures to biomaterials, Biopolymers 94 (1) (2010) 1–18. https://10.1002/bip.21328.
[58] Y.P. Liang, X. Zhao, T.L. Hu, B.J. Chen, Z.H. Yin, P.X. Ma, B.L. Guo, Adhesive hemostatic conducting injectable composite hydrogels with sustained drug release and photothermal antibacterial activity to promote full-thickness skin regeneration during wound healing, Small 15 (12) (2019) 17. https://10.1002/smll.201900046.
[59] W.B. Zhang, W.J. Zhong, L. Wang, A signal-amplification circuit between miR-218 and Wnt/β-catenin signal promotes human adipose tissue-derived stem cells osteogenic differentiation, Bone 58 (2014) 59–66. https://10.1016/j.bone.2013.09.015.
[60] M.M. Zhai, Y. Zhu, M.Y. Yang, C.B. Mao, Human mesenchymal stem cell derived exosomes enhance cell-free bone regeneration by altering their miRNAs profiles, Adv. Sci. 7 (19) (2020) 15. https://10.1002/advs.202001334.
[61] Y.K. Ju, Y. Hu, P. Yang, X.Y. Xie, B.R. Fang, Extracellular vesicle-loaded hydrogels for tissue repair and regeneration, Mater. Today Bio 18 (2023) 28. https://10.1016/j.mtbio.2022.100522.
[62] Y.X. Wang, Z. Cao, Q. Wei, K. Ma, W.Z. Hu, Q.L. Huang, J.L. Su, H.H. Li, C. P. Zhang, X.B. Fu, VH298-loaded extracellular vesicles released from gelatin methacryloyl hydrogel facilitate diabetic wound healing by HIF-1a-me diate d enhancement of angiogenesis, Acta Biomater. 147 (2022) 342–355. https://10.1016/j.actbio.2022.05.018.
[63] J.K. Zhang, J. Pan, W. Jing, Motivating role of type H vessels in bone regeneration, Cell Prolif. 53 (9) (2020) 10. https://10.1111/cpr.12874.
[64] A.J. Majmundar, W.H.J. Wong, M.C. Simon, Hypoxia-inducible factors and the response to hypoxic stress, Mol. Cell 40 (2) (2010) 294–309. https://10.1016/j.molcel.2010.09.022.
[65] X.G. Yu, X.H. Wang, D.J. Li, R.L. Sheng, Y.F. Qian, R. Zhu, X.D. Wang, K.L. Lin, Mechanically reinforced injectable bioactive nanocomposite hydrogels for in-situ bone regeneration, Chem. Eng. J. 433 (2022) 16. https://10.1016/j.cej.2021.132799.
[66] M.H. Chen, M.H. Li, X.J. Ren, F. Zhou, Y.A. Li, L. Tan, Z. Luo, K.Y. Cai, Y. Hu, DNAzyme nanoconstruct-integrated autonomously-adaptive coatings enhance titanium-implant osteointegration by cooperative angiogenesis and vessel remodeling, ACS Nano 17 (16) (2023) 15942–15961. https://10.1021/acsnano.3c04049.
[67] Y.A. Li, X.M. Liu, B. Li, Y.F. Zheng, Y. Han, D.F. Chen, K.W.K. Yeung, Z.D. Cui, Y. Q. Liang, Z.Y. Li, S.L. Zhu, X.B. Wang, S.L. Wu, Near-infrared light triggered phototherapy and immunotherapy for elimination of methicillin-resistant Staphylococcus aureus biofilm infection on bone implant, ACS Nano 14 (7) (2020) 8157–8170. https://10.1021/acsnano.0c01486.
[68] W.S. Lian, J.Y. Ko, Y.S. Chen, H.J. Ke, C.K. Hsieh, C.W. Kuo, S.Y. Wang, B. W. Huang, J.G. Tseng, F.S. Wang, MicroRNA-29a represses osteoclast formation and protects against osteoporosis by regulating PCAF-mediated RANKL and CXCL12, Cell Death Dis. 10 (2019) 14. https://10.1038/s41419-019-1942-1.
[69] Y. Qian, X. Zhou, F. Zhang, T.G.H. Diekwisch, X. Luan, J. Yang, Triple PLGA/PCL scaffold modification including silver impregnation, collagen coating, and electrospinning significantly improve biocompatibility, antimicrobial, and osteogenic properties for orofacial tissue regeneration, Acs Appl Mater Inter 11 (41) (2019) 37381–37396. https://10.1021/acsami.9b07053.
[70] Z. Wang, H. Li, H. Luo, H. Wang, Z. Ling, D. Chen, Q. Feng, X. Cao, Extracellular vesicles loaded dual-network bioactive sealant via immunoregulation and annulus

fibrosus repair for intervertebral disc herniation, J. Mater. Sci. Technol. 184 (2024) 75–87, https://doi.org/10.1016/j.jmst.2023.10.034.

[71] M. Segarra, M.R. Aburto, F. Cop, C. Llaó-Cid, R. Härtl, M. Damm, I. Bethani, M. Parrilla, D. Husainie, A. Schänzer, H. Schlierbach, T. Acker, L. Mohr, L. Torres-Masjoan, M. Ritter, A. Acker-Palmer, Endothelial Dab1 signaling orchestrates neuro-glia-vessel communication in the central nervous system, Science 361 (6404) (2018) 15. https://10.1126/science.aao2861.

[72] H.T. Pan, H.C. Gao, Q.T. Li, Z.F. Lin, Q. Feng, C.X. Yu, X.H. Zhang, H. Dong, D. F. Chen, X.D. Cao, Engineered macroporous hydrogel scaffolds via pickering emulsions stabilized by MgO nanoparticles promote bone regeneration, J. Mater. Chem. B 8 (28) (2020) 6100–6114. https://10.1039/d0tb00901f.